# Correlation between magnetic and crystal structural sublattices in palladium-doped FeRh alloys: Analysis of the metamagnetic phase transition driving forces

Aleksei S. Komlev[a,*], Dmitriy Y. Karpenkov[a,d], Radel R. Gimaev[a], Alisa Chirkova[e], Ayaka Akiyama[b], Takafumi Miyanaga[b], Marcio Ferreira Hupalo[f], D.J.M. Aguiar[g], A.M.G. Carvalho[h,i], M. Julia Jiménez[c], Gabriela F. Cabeza[c], Vladimir I. Zverev[a], Nikolai S. Perov[a]

[a] Faculty of Physics, M.V. Lomonosov Moscow State University, 119991 Moscow, Russia
[b] Department of Mathematics and Physics, Hirosaki University, Hirosaki, Aomori 036-8561, Japan
[c] Departamento de Física, Universidad Nacional del Sur, IFISUR (UNS-CONICET), Bahía Blanca, Argentina
[d] National University of Science and Technology "MISiS", 119049 Moscow, Russia
[e] TU Darmstadt, Institute for Materials Science, 64287 Darmstadt, Germany
[f] Materials Engineering Department, State University of Ponta Grossa - UEPG, Av. Gal. Carlos Cavalcanti, 4748, Ponta Grossa, PR 84030-900, Brazil
[g] Mechanical Engineering Department, Federal University of Technology – Parana (UTFPR), Doutor Washington Subtil Chueire St., 330, Ponta Grossa, PR 84017-220, Brazil
[h] Departamento de Engenharia Mecânica, Universidade Estadual de Maringá, 87020-900, Maringá, PR, Brazil
[i] Departamento de Engenharia Química, Universidade Federal de São Paulo, 09913-030, Diadema, SP, Brazil

## ARTICLE INFO

## ABSTRACT

FeRh alloys doped with the third element exhibit a change in the lattice and magnetic subsystems, which are manifested in antiferromagnetic- ferromagnetic (AFM-FM) first-order phase transition temperature, the shrinkage of the temperate hysteresis under transition, and the reduction of the saturation magnetization. All aforementioned parameters are crucial for practical applications. To control them it is quite important to determine the driving forces of the metamagnetic transition and its origins. In this manuscript ab initio calculations and experimental studies results are presented, which demonstrate the correlation between the structural and magnetic properties of the $Fe_{50}Rh_{50-x}Pd_x$ alloys. The qualitative analysis of the meta-magnetic phase transition driving forces in palladium-doped FeRh alloys was performed to determine their contribution to the evolution of magnetic and lattice subsystems. In addition, the impact of the impurities phases together with its magnetic behavior on the AFM-FM phase transition was considered.

© 2021 Elsevier B.V. All rights reserved.

## 1. Introduction

Near-equiatomic FeRh alloys ($Fe_{47}Rh_{53}$-$Fe_{53}Rh_{47}$) have been studied for more than 80 years, the first work was published by Fallot [1] in 1938. The continued interest of the scientific community in studying the family of these alloys is due to huge anomalies in magnetothermal, magnetotransport and magneto-volume properties in the vicinity of the first-order phase transition from antiferromagnetic (AFM) to ferromagnetic (FM) state, occurred near room temperature [2,3].

Despite the intensive and comprehensive study of these compounds, the origin of AFM-FM transition is still not completely clear. The first attempt to describe theoretically the magnetostructural transition was made by Kittel in the framework of the exchange inversion theory [4]. According to more recent theories [5–7], the phase transition in FeRh alloy is realized due to the occurrence of a magnetic moment on the Rh atom, that was observed experimentally. In turn, the presence of two magnetic states of Rh atoms is governed by competing FM Fe-Rh and AFM Fe-Fe exchange interactions [8]. The ferromagnetic order starts nucleating when the spin fluctuations of Fe sublattice in the antiferromagnetically ordered FeRh phase (α'' phase) induce a local exchange field on the Rh cites. The indirect ferromagnetic exchange mediated by the induced Rh magnetic moments overcomes the direct antiferromagnetic Fe-Fe exchange interactions, shifting the overall balance in favor of the

ferromagnetic order. The equilibrium lattice constant of the ferromagnetically ordered state is larger than that of the AFM state. Consequently, the AFM-FM transformation is accompanied by lattice expansion and stress relaxation. [6]. Such a theoretical prediction is approved by neutron diffraction studies and Mössbauer spectroscopy: it is known that in the FM phase there is a collinear ordering of magnetic moments of Fe atoms (3.2 $\mu_B$/atom) and Rh (0.9 $\mu_B$/atom) [9,10]. The magnetic moment of Fe atoms in the AFM phase is 3.3 $\mu_B$ [2], whereas Rh does not possess a magnetic moment [11,12].

Another approach, based on Monte Carlo calculations, was used in [13,14] to study the main factors responsible for the initiation of the phase transition. In [13] the influence of volume and spin fluctuations on the process of changing the magnetic state from AFM to FM was studied. As a result, based on the Landau-Heisenberg model, it was concluded that both spin and bulk fluctuations of the system are important for the transition in the alloy to occur. In [14] the main factors responsible for the magnetostructural transition were determined: the parameters of the exchange interaction between Fe atoms depend on the degree of magnetic ordering of the system and the value of the induced magnetic moment on Rh atoms.

To elaborate the contribution of each factor in the nucleation and evolution of the metamagnetic phase transition that occurred in these compounds several approaches to variate magnetic moments on the Rh cites and to distort crystal structure were applied. In order to shift the phase transition temperature, which acts as a marker of variations in the exchange energy of the systems, it is sufficient to apply a pressure/stress [15–18] or to dope the alloy with a third element [8,19–21]. The latter simultaneously leads to a change in the crystal structure and magnetic moment. At present, the properties of Pt-, Ir- and Pd-doped alloys were studied in [8,19,22], [16,20,23] and [19,23–27], correspondingly. Worth noted that in contrast to Pd-doping the substitution of the Rh atoms with the Pt and Ir atoms leads to an increase in the phase transition temperature. Ni-doped alloys were examined in [18,23]. As a rule, the high doping level with the third element can cause changes in the symmetry of the crystal lattice from body-centered cubic (bcc) to tetragonal (bct) or orthorhombic crystal structure [8,28]. The confirmation of the change in the crystallographic symmetry of Pd-doped FeRh alloys has been demonstrated using various experimental techniques: XRD (X-ray diffraction) [8,28–30], MFM (magnetic force microscopy) [31,32], XPEEM (X-ray photoemission electron microscopy) [32], neutron diffraction analysis [27]. However, the most precise technique for determining structural data is EXAFS (extended X-ray absorption fine structure), which was used to accurately describe the crystal structure of the binary FeRh alloys [33,34].

The correlation between magnetic and lattice subsystems in the series of FeRh-based compounds was additionally theoretically and experimentally explored. In particular, in [33] unexpected features in a FeRh α-phase structure has been found: the 2nd nearest Fe-Fe and Rh-Rh bond lengths are longer than that expected for the 1st nearest Fe-Rh or Rh-Fe bcc structure above the AFM-FM transition temperature. The same phenomenon was also reported recently in [34] for FeRh thin films. The observed results allowed the authors to conclude that the local magnetic moment (magnetic fluctuations) and Fe-Fe distance fluctuations (structural fluctuations) were revealed to play an important role in driving the metamagnetic transition, whereas the Fe-Rh atoms hybridization correlates with the static stability of each magnetic phase [34]. The most comprehensive and up-to-date consideration of the properties of alloys based on FeRh is given in the papers [35,36].

Another factor that can affect the magnetic behavior of FeRh-based alloys is homogeneity. As a rule, the synthesis of equiatomic FeRh alloys with guaranteed reproduction of properties is difficult. This is due not only to the difficulty in the preparation of a compound with elemental composition accuracy up to 0.1 at%, but also due to the presence of paramagnetic γ-phase in the sample, the

volume fraction of which may vary from units to tens of percent. The presence of γ-phase leads to redistribution of mechanical stresses on the α–γ phases interface during the phase transition, which can decrease the temperature of the phase transition [37]. Presumably, the appearance of the 'parasitic' phase is because its interface line on the concentration phase diagram passes near the values of synthesized concentrations [38]. In turn, due to finite cooling time during the as-cast specimen quenching, the system passes through a state in which the γ–phase is more stable. A detailed phase diagram has been constructed and described in [39]. In the same work, the influence of synthesis parameters on the formation of the γ-phase (annealing temperature, cooling time) was considered.

In turn, the magnetic behavior of the γ-phase is also controversial. Despite a majority of experimental works reporting the paramagnetic state of the former at room temperature [27,38,40], there are theoretical works that predict the stable FM state of the equiatomic FeRh γ-phase [41,42]. Moreover, in the experimental works [25,43] the spin-glass behavior of the γ-phase in bulk alloys and nanoparticles with fcc crystal structure has been reported. Therefore, the question of the magnetic ordering of the γ-phase and its contribution to the phase transition process remains open.

Here we try to elaborate the impact of all aforementioned factors on the AFM-FM phase transition to figure out the origin of the latter. This paper presents the results of ab initio and experimental exploration of magnetic properties and crystal structure. Via uniting the precise experimental techniques with theoretical calculation we shed the light on the correlation between the structural and magnetic properties of the palladium-doped Fe-Rh alloys and determine the main driving forces of the AFM-FM transition in the examined system.

## 2. Experimental

Since synthesizing the FeRh single-phase samples is challengeable [37,44,45], a method of sample preparation using arc melting was developed, which makes it possible to minimize the γ-phase with B1-type structure content in the sample. Alloys with the compositions of $Fe_{50}Rh_{50}$, $Fe_{50}Rh_{47}Pd_3$ and $Fe_{50}Rh_{45}Pd_5$ were synthesized by arc melting in an argon atmosphere. The adsorption of residual oxygen after evacuation in the chamber was carried out by melting a titanium getter.

To prevent the evaporation of the raw materials ingots during arc melting that can lead to a small deviation in the elemental composition of the target alloys, which in turn strongly affects magnetic properties [46], the formers were rearranged in the copper melting pot as shown in Fig. 1.

Each specimen underwent several melting followed with overturning to provide with even redistribution of the elements. The first
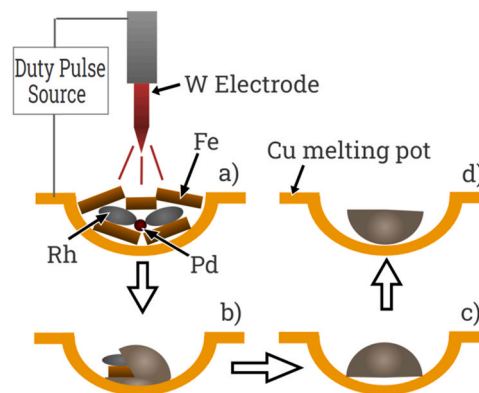


**Fig. 1.** a) The scheme of the Fe and Rh ingots arrangement before melting; b–d) illustrate the process of remelting, followed by sample overturning.

melting was performed at a low current, and the next four melts were performed at high current values. Increasing the arc current promotes the convection of the molten alloy. Reversing the sample after each melt homogenizes the sample. The obtained ingots were thermally treated for 24 h at 1273 K and then water-quenched. The described synthesis method made it possible to ensure a satisfactory quality of the alloys in this study (or within the set issue). The element composition of the alloy was determined by an electron probe microanalyzer EPMA (JEOL JXA-8800RL, JEOL Ltd.). The real values of the element concentrations in the samples: $Fe_{50.4}Rh_{49.6}$, $Fe_{49.7}Rh_{47.4}Pd_{2.9}$, and $Fe_{48.3}Rh_{46.8}Pd_{4.9}$.

The crystal structure of the prepared Fe(Rh,Pd) alloys was analyzed using XRD using the X-ray diffractometer (M18XHF-SRA, MAC Science Co. Ltd.) with Cu Kα line. The lattice parameters at 240 K of α"-phase for $Fe_{50.4}Rh_{49.6}$, $Fe_{49.7}Rh_{47.4}Pd_{2.9}$ and $Fe_{48.3}Rh_{46.8}Pd_{4.9}$ samples are 2.988 Å, 2.989 Å and 2.991 Å, respectively. Detailed information on X-ray diffraction data can be found in [27].

Metallographic preparation of the samples for EBSD analyzes was performed by mechanical polishing, using a commercial colloidal silica suspension. The results were determined by automatic indexing of Kikuchi patterns after adequate image processing in an EBSD (electron backscatter diffraction) AZtechHKL system coupled to a field emission gun scanning electron microscope (FEG-SEM) operating at 15 kV.

The Fe K-edge XAFS were obtained at BL9C in KEK (High Energy Accelerator Research Organization), Tsukuba with transmission mode. The Pd K-edge XAFS were obtained at NW10A in PF-AR, KEK detected by MSSD (Multi Element Sold State Detector) and BL11S2 in Aichi SR center detected by SDD (silicon drift detector) with fluorescence mode. XAFS analyses were performed by Athena and Artemis code[47].

Macroscopic magnetic measurements were studied using the VSM Lakeshore 7407 Series over a wide temperature range (80–450 K). Heating and cooling of the sample were carried out at a rate of 2 K/min, overheating did not exceed 0.5 K. The selection of the temperature, at which it is correct to compare the magnetization of the alloys with different Pd–doping levels, is the main problem. Since the samples have different field-dependent temperatures of the AFM-FM phase transition, a measurement procedure was developed that allows one to carry out a reasonable analysis of the magnetic properties. First, it is necessary to measure the temperature dependence of the magnetization in the same field, which exceeds the saturation field of all samples. On the minus side, the presence of the external magnetic field will decrease the AFM-FM phase transition temperature, but on the other hand, measurements at low fields are not able to provide information on the saturation magnetization of the samples. The obtained curve was used to find the temperature at which the zeroing out of the magnetization derivative is realized ($T_{dM/dT=0}$). This temperature ensures the "maximum ferromagnetic" state of the system, because at lower temperatures the coexistence of the AFM and FM phases is observed in the alloy, and at high temperatures the sample starts demagnetizing due to magnetic moments thermal fluctuations. An illustration of the measuring and determining the saturation magnetization procedure is given in the Supplementary material in Fig. S1. After determining the magnetic moment of the sample at a given temperature, it is necessary to normalize the measured value by the volume of the ferromagnetic phase. Since γ–phase is paramagnetic for FeRh alloys near the room temperature [27,38], the magnetization was recalculated for the volume of the α'-phase, the percentage of which was determined from EBSD analysis.

## 2.1. Computational details

Spin-polarized calculations were carried out using VASP (Vienna *Ab-Initio* Simulation Package) code [48–50] within the formalism of the Density Functional Theory. In the standard mode, VASP performs a fully relativistic calculation for the core-electrons and treats valence electrons in a scalar relativistic approximation [51]. The energy convergence criterion used was 0.1 meV. The kinetic energy cut-off for the plane wave expansion of the Kohn-Sham electronic wave function is 400 eV. The plane wave basis was generated considering 8 valence electrons for Fe ($3d^7 4s^1$), 9 valence electrons for Rh ($4d^8 5s^1$) and 10 valence electrons for Pd ($4d^9 5s^1$).

The Projector Augmented-Wave (PAW) method [52] was used to reproduce the atomic core effects in the electronic density of the valence electrons. The exchange and correlation energies were calculated with the Generalized Gradient Approximation due to Perdew, Burke and Ernzerhof [53].

Two types of the crystal structure of FeRh Pd-doped bulk alloy were studied: a B2 CsCl-type structure and B1 CuAu-type structure which corresponds to α-phase and γ-phase [27]. For the first structure, both ferromagnetic (FM) and antiferromagnetic (AFM) spin configurations were studied. In order to facilitate comparison with experimental results, the alloy was represented using (4 × 4 × 4) supercell formed by 128 atoms to obtain Pd concentrations close to the experimental values of 2.9 and 4.9. Half of them correspond to Fe atoms and the other half consists of Rh atoms where some Rh are replaced by Pd atoms depending on the concentration. The nomenclature used to represent the different systems studied is $Fe_{50}Rh_{50-x}Pd_x$ (x = 0, 2.3, 4.7). In the case of the B1 type structure, the FM and paramagnetic configurations were studied. According to experimental evidence, it is known that the B1 phase should be paramagnetic [27,38]. However, earlier the problem of the possibility of the ferromagnetic ordering of this structure was considered [41]. Therefore, the reasons for the observation of the paramagnetic state are still unclear. The calculation of the paramagnetic phase was carried out in two ways. In the first case, a non-spin polarization model (NM) was used, just as it was done in the work [41]. In the second case, the magnetic moments on the atoms were randomly oriented in such a way that the total magnetic moment was zero (PM). In this case the supercell used is a (3 × 3 × 3) formed by 108 atoms, half of them correspond to Fe atoms and the other half are Rh atoms substituted with Pd to obtain $Fe_{50}Rh_{47.2}Pd_{2.8}$ and $Fe_{50}Rh_{45.4}Pd_{4.6}$ concentrations. The configurations are shown in Fig. 2. The procedure followed for the modeling of the FM and AFM configurations for the B2-type case was recently studied/published by our group for other Pd concentrations [42]. In the case of the B1-type structure, the initial cell parameter (a = 3.752 Å) was obtained from published results [54]. All the initial structures studied including doping started from the same cubic unit cell allowing total relaxation in all directions to simplify comparison. The Brillouin zone (BZ) integration was performed on well-converged Monkhorst-Pack [54] k-point meshes of (5 × 5 × 5).
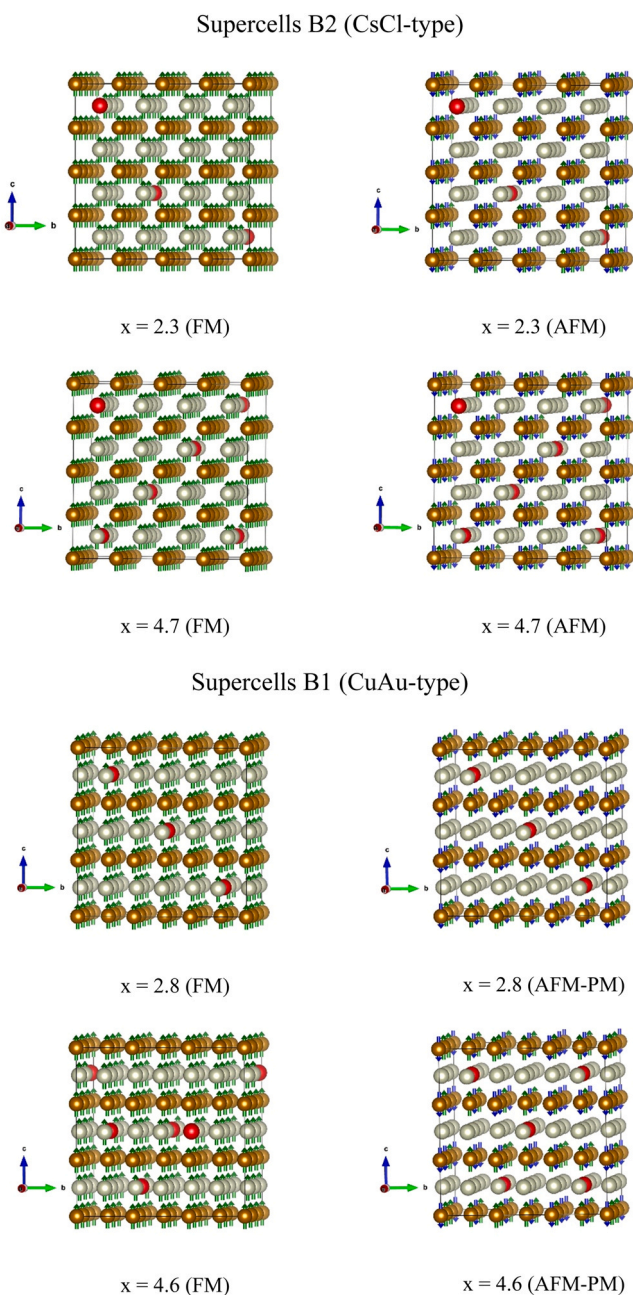
The corresponding density of states (DOS) and local density of orbital states (LDOS) were computed [55]. The magnetic moments per atom ($\mu_B$/at.) for both α'-and γ-phases in the FM state were obtained to complete the analysis.

## 3. Theoretical consideration

### 3.1. Structural and magnetic properties

Two values of Pd-doping x = 2.3 and 4.7 corresponds to those obtained experimentally x = 2.9 and 4.9. For FM-B2 structure (α'-phase), the lattice constants calculated for $Fe_{50}Rh_{50}$ and $Fe_{49.7}Rh_{47.4}Pd_{2.9}$ are 3.004 Å and 3.005 Å; in turn, for $Fe_{48.3}Rh_{46.8}Pd_{4.9}$ a slight distortion of the cubic cell to a tetragonal one is observed with a ration c/a = 0.98 (a = 3.041 Å; c = 2.991 Å); the corresponding lattice parameters for AFM-B2 (α"-phase) are 2.987 Å, 2.988 Å and 2.992 Å for $Fe_{50}Rh_{50}$, $Fe_{49.7}Rh_{47.4}Pd_{2.9}$ and $Fe_{48.3}Rh_{46.8}Pd_{4.9}$, respectively. For the same Pd concentrations, the corresponding lattice

## Supercells B2 (CsCl-type)



x = 2.3 (FM)

x = 2.3 (AFM)

x = 4.7 (FM)

x = 4.7 (AFM)

## Supercells B1 (CuAu-type)

x = 2.8 (FM)

x = 2.8 (AFM-PM)

x = 4.6 (FM)

x = 4.6 (AFM-PM)

**Fig. 2.** Models of supercells used to represent different Pd concentrations in $Fe_{50}Rh_{50-x}Pd_x$ alloy B2 (CsCl-type) (x = 0, 2.3, 4.7) and B1 (CuAu-type) (x = 0, 2.8, 4.6). The Pd concentration (x) is indicated below each cell. Color reference: Rh atoms are in gray, Pd atoms are in red and Fe atoms are in gold. Arrows (spin up and spin down) indicate magnetic moments.

parameters are 3.787 Å, 3.794 Å and 3.802 Å for FM-B1 and 3.680 Å, 3.682 Å and 3.684 Å for NM-B1 and 3.843 Å, 3.852 Å and 3.854 Å for PM-B1. The calculated parameters of the crystal lattice correlate with the experimental results observed for these samples in the previous work [27]. An insignificant increase in the crystal lattice parameter of γ-phase may be due to the lack of taking into account the spin-orbit interaction in the case of theoretical calculations.

The works [8,27,28,32] reported on the tetragonalization of the FeRh α'-phase crystal lattice upon the addition of Pd. To analyze the structure and compare it with XAFS results, interatomic distances were calculated. The variation of the first nearest neighbor (NN) Pd-Fe distance obtained from optimization for $Fe_{50}Rh_{47.7}Pd_{2.3}$ and $Fe_{50}Rh_{45.3}Pd_{4.7}$ are around 0.03 Å. In the case of the B1 structure the Pd-Rh NN distances (both atoms are in the same 001 plane) vary

between 0.04/0.05 Å. However, no great variations are observed in the Pd-Fe distances (0.01 Å).

In Fig. 3, the total energies per atom are plotted to be able to compare the different supercells used. In the case of B2 structure, the antiferromagnetic ordering is a bit stable than the ferromagnetic one by 0.03 eV (see Fig. 3(b)). For B1 structure the energy was calculated considering both spin polarization (FM), non-spin polarization (NM), and random orientated spin moments (PM). In this case, the ferromagnetic ordering of magnetic moments is more stable than NM state by a tenth of eV, growing barely as x increases (0.13/0.14/0.15 eV). But the calculation of the paramagnetic phase using the method of randomly oriented spins (PM) showed that such a state is more stable than the ferromagnetic one. Worth noting that for both B1 and B2 structures an increase in the total energy of the system is observed when Rh is substituted with Pd. The calculation of the energy for the paramagnetic phase using the method of randomly oriented spins gave a result that is consistent with the experiment.

In Fig. 4 the magnetic moment ($\mu_B$ per atom) of Fe, Rh and Pd atoms are depicted for α'-and γ-phases in the FM state with B2 and B1 structures, respectively. As shown, in the case of the B2 structure the values of Fe moments slightly decrease $\mu$ = 3.18, 3.17 and 3.16 $\mu_B$/Fe within the Pd concentration growth of 0%, 2.3% and 4.7% correspondingly. In contrast, in the B1 structure the magnetic moment values raise (2.53, 2.60 and 2.64 $\mu_B$/Fe).

In turn, the values of magnetic moment per Rh atoms differ in the order of magnitude for B1 and B2 structures. In the case of Pd atoms, the values are similar and equal to 0.2 $\mu_B$/Pd and 0.3 $\mu_B$/Pd for the B1 and B2 structures, respectively. As a result, the total magnetization per atom in a supercell decreases and increases with the Pd doping for the B2 and B1 structures, respectively (Fig. 4, right axis). The experimental values of the magnetic moments per atom in the considered compounds obtained by means of neutron diffraction are presented in [27] and coincide well with the calculated results in the case of B2 structure. It is worth noting that the neutron diffraction studying does not answer the question is the revealed change in the total magnetization per unit cell guided by a change in the magnetic moment of the Fe atom either a change in the fraction of the ferromagnetic magnetic phase above AFM-FM transition. The presented simulation points out that in the ferromagnetic state, the decrease in the magnetic moment per unit cell is associated with a decrease in the magnetic moment of Fe atoms.

The revealed decrease in the magnetic moment per Fe atom with increasing Pd concentration in the B2 structure is a consequence of the exchange integral decrease due to the crystal structure tetragonalization. This reduction causes the decrease of the AFM-FM transition temperature due to lower contribution from the magnetic subsystem in the total free energy. According to [13] one should take into account two types of competing energies when considering a magnetic first-order phase transition in such a system: the contribution arising from the lattice degrees of freedom (phonon energy) and the spin subsystem energy. At high temperatures, the thermal energy dominates, and the system enters a paramagnetic state. At temperatures below the Curie temperature the system can be either in the AFM or FM state depending on the distance between the atoms, which can be tuned by temperature or by an external magnetic field. Thus, a decrease in the exchange constant, which depends on the interatomic distance, leads to a decrease in the thermal energy (phonon energy) required to change the ordering of the spin subsystem.

### 3.2. Electronic properties

To complete the analysis, the corresponding electronic structures for certain Pd concentrations have been calculated. The total (DOS) density of states for the FM and AFM and NM and FM magnetic
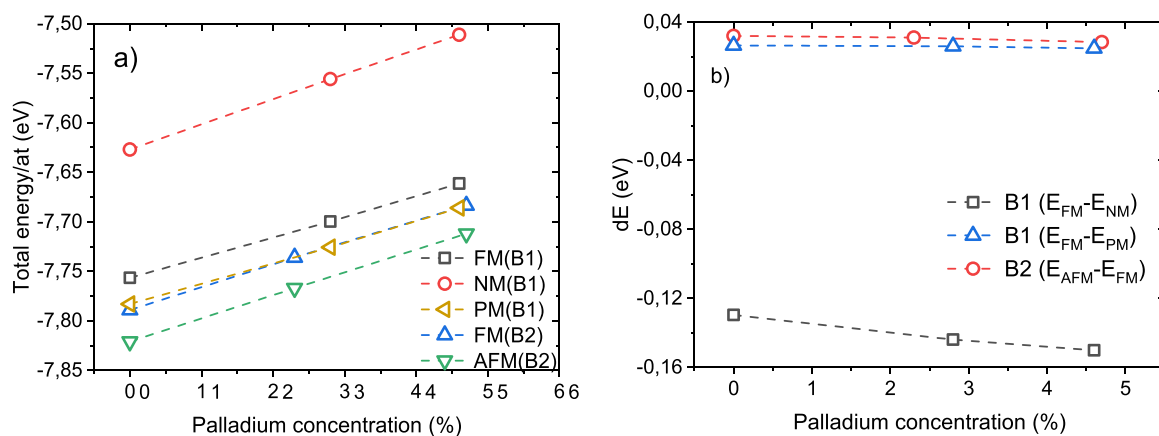
**Fig. 3.** a) Calculated total energies as a function of Pd concentration for $Fe_{50}Rh_{50-x}Pd_x$ for B2 and B1 structures. b) Open circle symbols corresponds to the energy difference (dE) between the AFM phase and the FM phase in B2 structure; Open square symbols corresponds to the energy difference between the FM phase and the NM phase in B1 structure; Open triangular symbols corresponds to the energy difference between the FM phase and the PM phase in B1 structure.
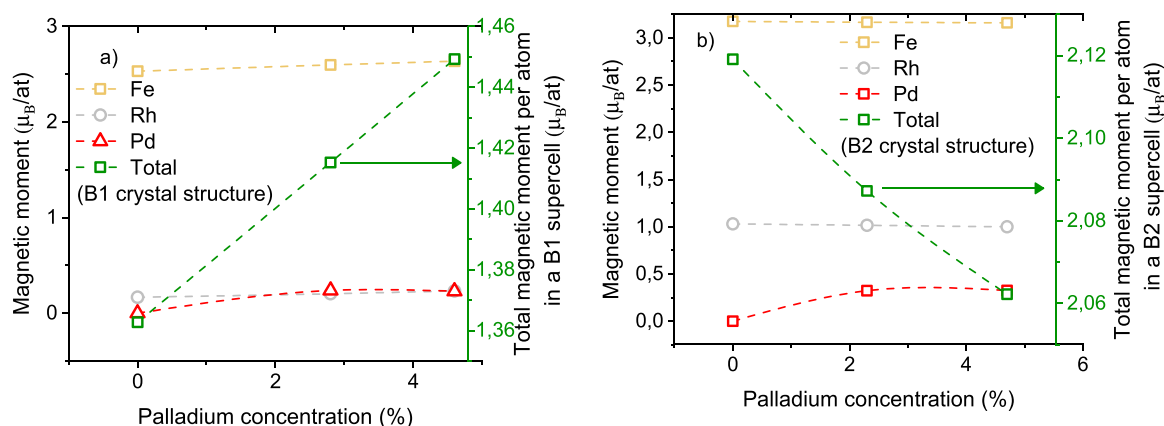


**Fig. 4.** Magnetic moments of the atoms for FM spin configuration at different Pd concentrations for a) B1 structure and b) B2 structure. The total magnetization per atom in a supercell is added (right axis).

configurations were calculated for B2 and B1 structures, respectively. The data are presented in Supplementary materials (Fig. S2, Fig. S3 correspondingly). As it is known, the balance between the spin-up and the spin-down states is the reason behind the anti-ferromagnetism of these systems. Previously the features in the magnetization of the Fe and Rh atoms for AFM and FM configurations were theoretically revealed by the members of our group [56]. These peculiarities were attributed to hybridization between Rh states with a given spin projection and the spin states of Fe on a local sub-lattice and in the same way with the spins down on another local sub-lattice. As a consequence, the net magnetic moment of the Rh atoms is zero in the AFM phase, while the Fe atoms possess values close to those they have in the FM phase. It is notable that the structure of maxima in the LDOS in AFM state for Fe sites reflects a strong spin polarization, as in the FM case. This may also indicate that the Rh atoms do not average the influence of two opposite states of Fe, but that the Rh atoms hybridize locally with the spin states around them, i.e., a greater overlap between themselves takes place. Similar behavior is observed in the value of the magnetic moment of the Pd (located in Rh sites) that goes from 0.3 (FM) to $0\,\mu_B/Pd$ (AFM). Therefore, the formation of the magnetic moment of the Rh/Pd is governed by the strong covalence between them and the polarized spin states of the first neighboring Fe atoms. The influence of the type of structure is also manifested in the B1 case where the first neighbors are some Fe (upper and lower planes) and Rh in the same plane. When substituting Rh with Pd, the magnetic moments are practically unchanged (around $0.2\,\mu_B/at$) (Fig. 4b).

In the case of the B1 structure the calculations were carried out to elaborate the magnetic behavior of the $\gamma$–phase. For better visualization, the LDOS of the Pd $4d$ states per Pd atom near Fermi energy were plotted for different Pd content for both structures in the FM state (see Fig. 5). The comparison analysis of Fe LDOS at the Fermi level in the NM phase for the B1 structure has revealed its large local values (see Fig. 3S). This can point out the instability of this phase towards the ferromagnetism and indicates a higher local magnetic moment of Fe atoms compared to the Rh and Pd ones as has been previously commented (Fig. 4a).

Spin polarization and spin polarization of electrons at the Fermi energy on Pd atoms were calculated for both structures with a certain Pd-doping level, the results are presented in Table 1. Integrating the local densities of electron states was performed in the range from − 10 to 0 eV (across all populated electronic levels). The spin polarization per atom in the B1 lattice is smaller than in the B2 structure. This fact can be another reason for the absence of ferromagnetic ordering in the B1 structure. An increase in the palladium concentration leads to a decrease in the polarization of palladium $d$ electrons, which is explained by a change in the effective field of the crystal. The electronic properties at the Fermi level play an essential role in understanding the magnetic properties of materials. One way to quantify the difference between spin-up and spin-down components is by evaluating spin polarization at the Fermi level. In the case of B2 structure, the largest spin polarization at the Fermi energy is a consequence of the large spin-down DOS compared to the spin-up component at the Fermi level implying that all the structures exhibit
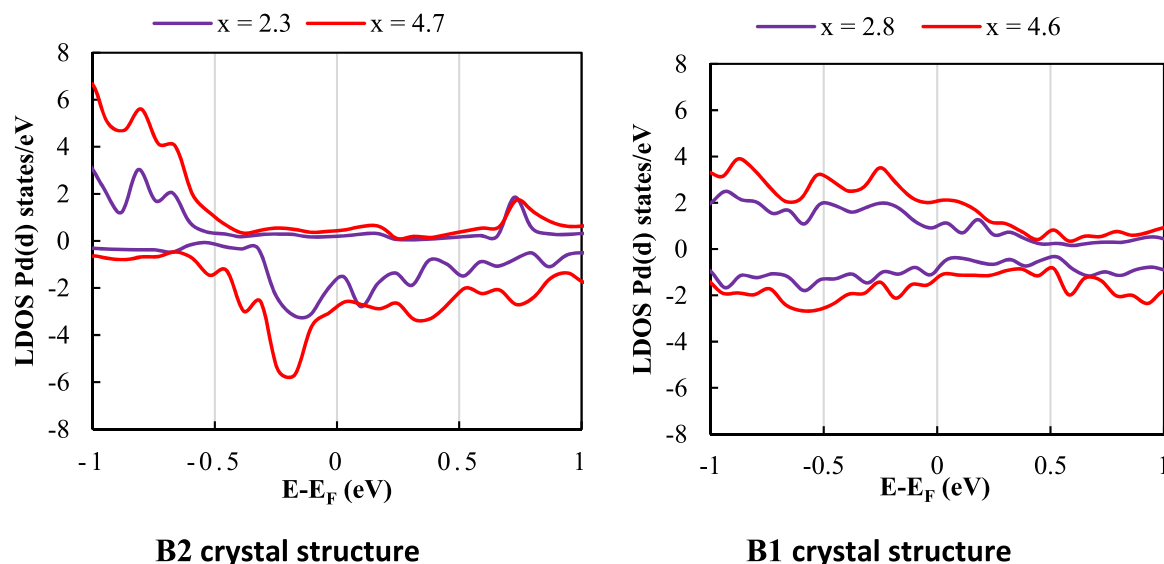
**Fig. 5.** Local Pd-4d states in the B2-FM state (left) and B1 -FM states (right) at different contents of Pd. The spin-down (minority) LDOS were plotted as negative values.

**Table 1**
Calculated parameters of local Pd-4d states in the (B2, B1)-FM state at different contents of Pd. Here $\rho_\uparrow$ and $\rho_\downarrow$ are the total density of states of the spin-up and spin-down bands respectively, P is spin polarization, $P(E_f)$ is spin polarization at the Fermi energy.

| x (Pd), % | 2.3 for B2, 2.8 for B1 | | | | 4.7 for B2, 4.6 for B1 | | | |
|---|---|---|---|---|---|---|---|---|
| | $\rho_\uparrow$ | $\rho_\downarrow$ | P $\frac{\rho_\uparrow - \rho_\downarrow}{\rho_\uparrow + \rho_\downarrow}$ | $P(E_f)$ $\frac{\rho_\uparrow(E_f) - \rho_\downarrow(E_f)}{\rho_\uparrow(E_f) + \rho_\downarrow(E_f)}$ | $\rho_\uparrow$ | $\rho_\downarrow$ | P $\frac{\rho_\uparrow - \rho_\downarrow}{\rho_\uparrow + \rho_\downarrow}$ | $P(E_f)$ $\frac{\rho_\uparrow(E_f) - \rho_\downarrow(E_f)}{\rho_\uparrow(E_f) + \rho_\downarrow(E_f)}$ |
| B2 | 14.52 | -13.37 | 0.041 | 0.69 | 29.78 | -28.34 | 0.024 | 0.75 |
| B1 | 14.62 | -13.66 | 0.034 | 0.42 | 24.43 | -23.4 | 0.021 | 0.32 |

ferromagnetic properties. In the case of the B1 configurations, the spin polarization values at the Fermi energy are smaller than in the case with B2 structure, that indicating similar contributions in the densities of up and down states. Therefore, this fact confirms the assumption that the B1 structure is in a paramagnetic state. The DOS curves' qualitative form for the FM configurations in B1 (Fig. S3) is similar in all studied structures (x = 0, 2.8 and 4.6) with strong hybridization between Fe 3d states and Rh 4d states. Unlike the B2 structure, the vicinity of the Fermi level is not only dominated by Fe 3d states but the presence of the Rh states 4d is also observed. Increases in Pd concentrations lead to slight changes in the densities of electronic states near $E_F$.

Summarizing, via ab-initial calculation the paramagnetic state for γ−phase (B1) was determined using two different approaches: total energy estimation and LDOS diagram constructing.

Additionally, a tendency for the spin polarization on Pd atoms to decrease as their (Pd) concentration increases are observed for both structures. This result is explained by a decrease in the value of s-d hybridization due to a decrease in the number of Rh atoms that possess an unpaired s-electron on the outer shell.

## 4. Experimental results and discussion

### 4.1. Structural analysis

#### 4.1.1. EXAFS

The distortion of the crystal lattice under substitution of Rh with Pd, theoretically predicted in the previous section and experimentally demonstrated via neutron diffraction in [27], was studied in detail by EXAFS analysis in this chapter. Temperature dependence of $k^3\chi(k)$ and Fourier transform (FT) of Fe K-edge XAFS presented in Supplementary material (Fig. S4 and S5) and that of $k\chi(k)$ and FT of

Pd K-edge XAFS presented in S6 and S7. They show the local atomic structure around Fe atoms and Pd atoms, respectively. $\chi(k)$ – normalized EXAFS, which characterizes the relative changes in the photoionization cross sections in comparison with atomic ones due to the influence of the environment, k is the wave number of the photoelectron. Fourier analysis of the function $\chi(k)$ allows to determine the contributions of individual coordination spheres. In particular, the profiles of $k^3\chi(k)$ and FT Fe K-edge XAFS are almost similar to that of FeRh [33], which indicates the local structure around Fe in FeRhPd is similar to that in FeRh. Thus, our attention is focused to whether such behavior is also observed in Pd-doped FeRh alloys. Fig. 6 demonstrates temperature dependence of interatomic distances in $Fe_{49.7}Rh_{47.4}Pd_{2.9}$ and $Fe_{48.3}Rh_{46.8}Pd_{4.9}$ for (a) 1st nearest neighbor (NN) and (b) 2nd nearest neighbor obtained from the curve fitting with Artemis code [47]. In Fig. 6(a) the 1st NN distances are multiplied by $2/\sqrt{3}$ as required by the symmetry of the B2 structure. The 2nd NN distances are longer comparing with the 1st NN one similar to binary FeRh [33,34], that is the local distortion exists also in FeRhPd alloys analogously to binary systems. On the other hand, the distortion is found in the wider temperature range but not only above the AFM-FM transition temperature.

The interatomic Fe-Rh and Fe-Fe distances obtained from the Fe K-edge XAFS analysis for $Fe_{49.7}Rh_{47.4}Pd_{2.9}$ and $Fe_{48.3}Rh_{46.8}Pd_{4.9}$ are 0.02 Å longer compared with the corresponding values for $Fe_{50.4}Rh_{49.6}$ [33]. The local structure around Fe atoms obtained from XAFS experiments is almost the same as from XRD measurements taking the lattice constants values into account.

In turn, the Pd-Fe and Pd-Rh interatomic distances obtained from the Pd K-edge XAFS analysis for $Fe_{49.7}Rh_{47.4}Pd_{2.9}$ and $Fe_{48.3}Rh_{46.8}Pd_{4.9}$ are around 0.04 Å longer in comparison with the equivalent values of Rh-Fe and Rh-Rh interatomic distances for $Fe_{50.4}Rh_{49.6}$ [33]. Thus, the local structure distortion around Pd atom
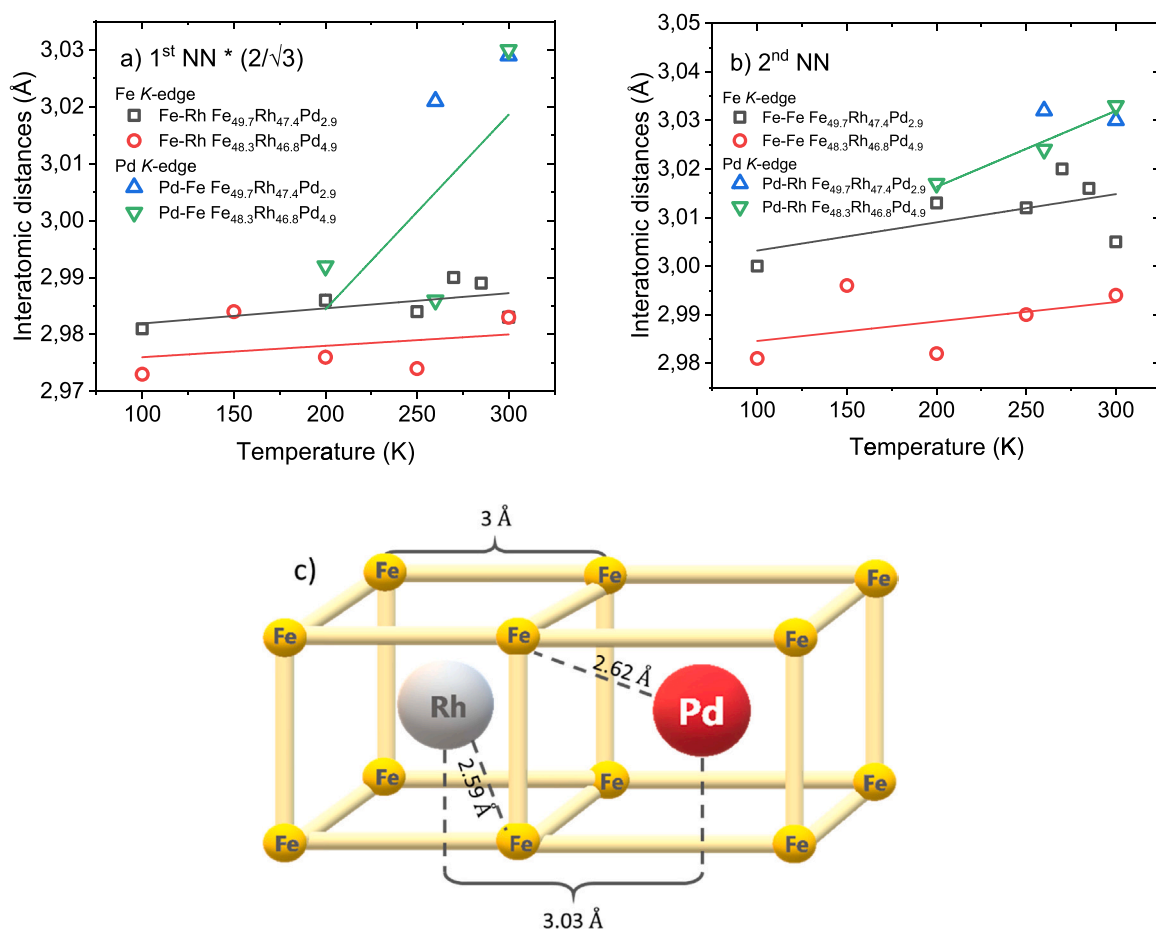
**Fig. 6.** Temperature dependence of interatomic distances in $Fe_{49.7}Rh_{47.4}Pd_{2.9}$ and $Fe_{48.3}Rh_{46.8}Pd_{4.9}$ for (a) 1st nearest neighbor (NN) and (b) 2nd NN. In (a), the 1st NN distances are multiplied by $2/\sqrt{3}$ for comparison. (c) Schematic illustration of the crystal lattice tetragonalization upon addition of palladium.

is more pronounced compared to the surroundings of Rh atoms in Pd-doped alloys. Moreover, the interatomic Pd-Fe and Pd-Rh distances increase more than Fe-Rh and Fe-Fe ones in the vicinity of the transition temperature. It means that the nucleation centers of a new phase in three-component systems are atoms located near palladium.

Thus, the substitution of rhodium for palladium leads to a local distortion of the crystal lattice (it's tetragonalization), resulting in a decrease in the distance between the iron atoms that are in the nearest neighborhood of the palladium. A schematic representation of the change in interatomic distances is shown in Fig. 6c. This distortion leads to an increase in the interatomic distance between the first and second nearest neighbors of palladium, which, in turn, reduces the magnitude of the exchange interaction between them. The presence of local tetragonalization of the crystal lattice and a decrease in the exchange interaction between the nearest iron atoms leads to a decrease in the phase transition temperature.

*4.1.2. Scanning electron microscopy*

As it was mentioned in the Introduction the presence of the impurities can strongly affect the magnetic behavior of FeRh-based alloys. In this chapter we experimentally study the influence of the Pd-doping on the γ-phase (B1 structure) volumetric content using EBSD analysis. The EBSD maps for FeRh and Pd-doped alloys are depicted in Fig. 7. The details of EBSD technique are described in Supplementary Material. The pattern quality maps (gray figures) offer good indexing of diffraction patterns. The slight blur observed in Fig. 7a does not compromise the quality of the mapping. For all pattern quality maps, dark areas indicate lower diffraction pattern

quality, while the lighter areas represent higher pattern quality. EBSD data allowed to identify the presence of three phases: alpha1 (blue), alpha2 (red), and gamma (yellow), in all studied alloys. The legend for each phase is described elsewhere [57]: alpha 1 is an antiferromagnetic α"-phase being a variation of the ferromagnetic one (B2 structure), alpha 2 is ferromagnetic α'-phase (B2 structure) and γ-phase (B1 structure). Worth noted, that the alpha 2 phase (red) is preferably located at alpha1-grain boundaries or alpha1/gamma interfaces (Fig. 7). This fact confirms the assumption that the growth of a new phase nucleates on defects. Since the phase transition temperature of the binary FeRh alloy is near the room temperature, and the EBSD analysis was performed at 300 K, it is obvious that the coexistence of the alpha1 and alpha2 phases is observed on the map (Fig. 7a). The Pd-doping leads to a decrease in the AFM-FM transition temperature, so the alpha 2 phase is predominant (Fig. 7b,c) in $Fe_{49.7}Rh_{47.4}Pd_{2.9}$ and $Fe_{48.3}Rh_{46.8}Pd_{4.9}$ samples.

From the alpha 1, alpha 2, and gamma phases' areas (Fig. 7), the volume content of these phases was determined. Table 2 presents the corresponding phase fractions estimated from EBSD data. Seven images taken at different locations (picture size is 60 * 60 µm) were analyzed for each sample to reduce static error. The presented results demonstrate a decrease in the volume fraction of the γ-phase with Pd concentration increasing. Presumably, it can be attributed to the radius of the doping atom. Since the Rh atom is smaller than Pd one, the probability to substitute the atom on the face of the cubic B1 structure is less than in the body of B2 structure because of geometric reasons. Moreover, under an increase of the Pd concentration the equilibrium state is shifted to the stability of the α-phase, and together with the Fe concentration decrease within the
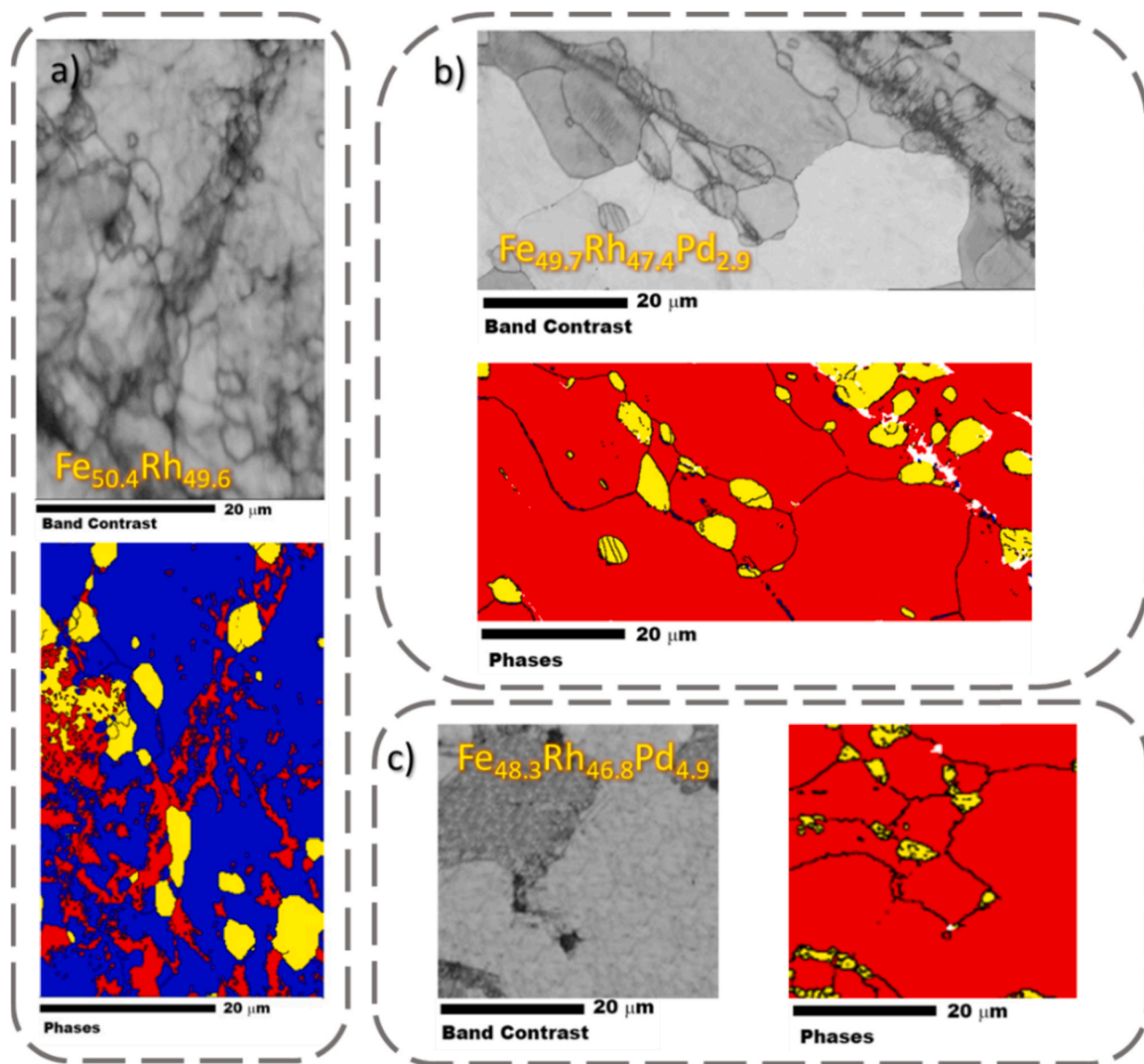
**Fig. 7.** EBSD data from a) $Fe_{50.4}Rh_{49.6}$, b) $Fe_{49.7}Rh_{47.4}Pd_{2.9}$, c) $Fe_{48.3}Rh_{46.8}Pd_{4.9}$ alloy. Gray pictures show the pattern quality map, color pictures are phase distribution maps (alpha 1-blue, alpha 2-red, gamma-yellow).

**Table 2**
Phase fraction quantified from EBSD data for $Fe_{50.4}Rh_{49.6}$, $Fe_{49.7}Rh_{47.4}Pd_{2.9}$, and $Fe_{48.3}Rh_{46.8}Pd_{4.9}$ alloys.

| Phase/color | $Fe_{50.4}Rh_{49.6}$ | $Fe_{49.7}Rh_{47.4}Pd_{2.9}$ | $Fe_{48.3}Rh_{46.8}Pd_{4.9}$ |
|---|---|---|---|
| Alpha 1/blue | 66.7% | 4.5% | 0.7% |
| Alpha 2/red | 26.0% | 90.7% | 93.2% |
| Gamma/yellow | 7.3% | 4.8% | 4.3% |

Pd-doping, make the former more stable. Unfortunately, most of the published works do not provide information on the percentage content of the γ-phase in FeRh-based ternary alloys.

The γ-phase inclusions size distribution diagrams were plotted using SEM images (Fig. 8). The number of analyzed inclusions for each of the samples exceeded 100. The resulting statistics were approximated by a Gauss distribution to determine the average size of the gamma-phase inclusion. The average inclusion sizes < D > are 6.3, 4.2, 3.3 μm for the $Fe_{50.4}Rh_{49.6}$, $Fe_{49.7}Rh_{47.4}Pd_{2.9}$ and $Fe_{48.3}Rh_{46.8}Pd_{4.9}$ alloys, respectively.

As shown the volume fraction of the γ-phase in Pd-doped alloys decreases due to a decrease in the average size of the inclusion. Additionally, the elemental composition of the γ-phase in each of the alloys was analyzed using EDX analysis, the results are presented in the Supplementary Material in Fig. S9. The percentage of iron does not exceed 39 at% in each case.

### 4.2. Magnetic measurements

The temperature dependences of magnetization were measured according to the protocol described in the Experimental. AFM-FM phase transition temperatures and saturation magnetization $\sigma_S$ values for the $Fe_{50.4}Rh_{49.6}$, $Fe_{49.7}Rh_{47.4}Pd_{2.9}$ and $Fe_{48.3}Rh_{46.8}Pd_{4.9}$ samples measured under an external magnetic field of H = 16 kOe are listed in Table 3.

Magnetization values were determined at temperatures where the magnetization derivative reaches zero value ($T_{dM/dT=0}$). The magnetization of the alloys decreases with increasing Pd concentration, as predicted theoretically in this paper. As shown in
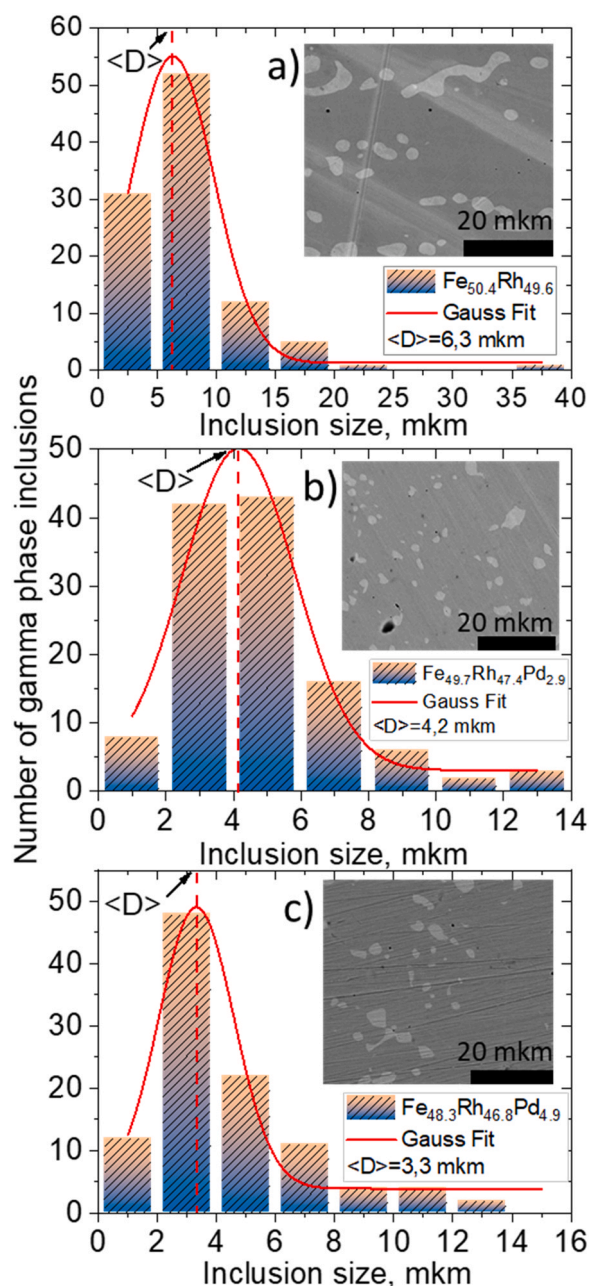
**Fig. 8.** The γ-phase inclusions size distribution for a) $Fe_{50.4}Rh_{49.6}$ b) $Fe_{49.7}Rh_{47.4}Pd_{2.9}$ c) $Fe_{48.3}Rh_{46.8}Pd_{4.9}$ samples. Inserts illustrate the BSE images of the corresponding samples.

**Table 3**
Magnetization and the main temperature parameters characterizing the phase transition of the samples.

|  | $T_{AFM-FM}$, K | $\sigma_S$,emu/g | $T_{dM/dT=0}$, K | $\Delta T$, K |
|---|---|---|---|---|
| $Fe_{50.4}Rh_{49.6}$ | 333 | 130 | 379 | 34.7 |
| $Fe_{49.7}Rh_{47.4}Pd_{2.9}$ | 295 | 127 | 354 | 33.8 |
| $Fe_{48.3}Rh_{46.8}Pd_{4.9}$ | 289 | 122 | 348 | 28.0 |

Fig. 9, two magnetization maxima are observed at different temperatures between the AFM and FM states, which correspond to the heating and cooling protocol of measurements. The high-temperature state was chosen for the analysis because the low-temperature state is metastable. Pd concentration rising leads to a decrease in the
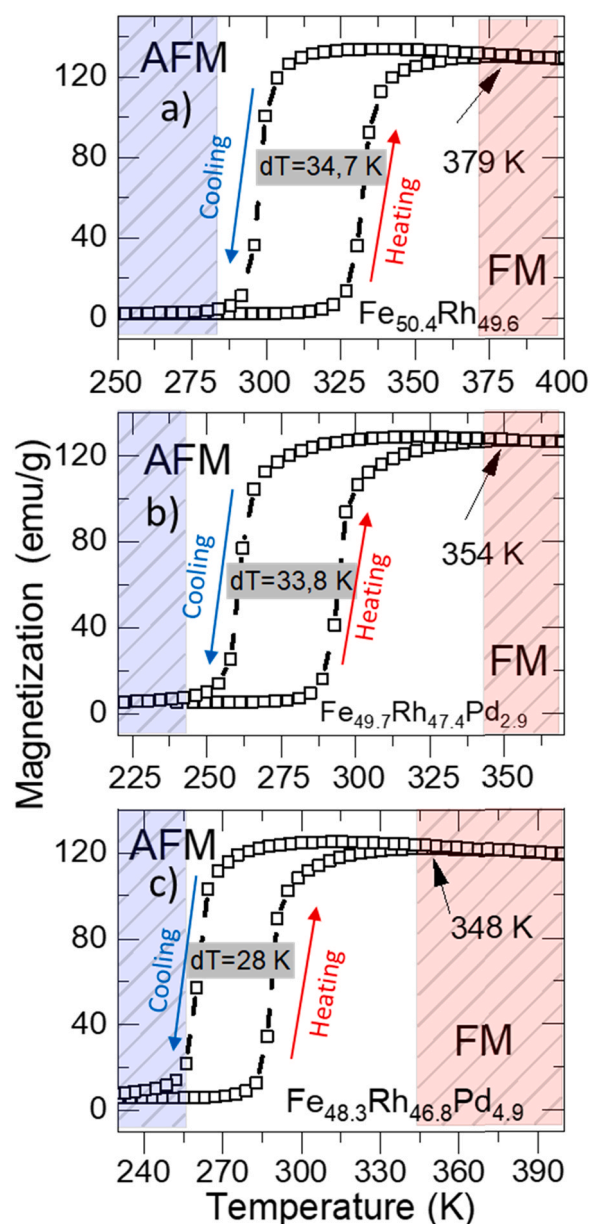


**Fig. 9.** Temperature dependencies of magnetization for (a) $Fe_{50.4}Rh_{49.6}$, (b) $Fe_{49.7}Rh_{47.4}Pd_{2.9}$ and (c) $Fe_{48.3}Rh_{46.8}Pd_{4.9}$ at 16 kOe.

phase transition temperature, which is consistent with previously published data and with the theoretical model described above. The temperature hysteresis width (ΔT in Table 3) also decreases under Pd-doping, which can be partially attributed to a decrease in the γ - phase volume fraction in the sample. The interfaces between the α''- and γ - phases are the pinning centers of the ferromagnetic phase during the phase transition. This statement was confirmed via the EBSD analysis results (Fig. 7), where one can see that the pinned clusters of the antiferromagnetic phase are predominantly located near the interfaces of the aforementioned phases. An increase in the number of such defects leads to a broadening of the temperature hysteresis. The contribution of the other intrinsic and extrinsic hysteresis origins [58] will be estimated in detail in further works. Moreover, the influence of crystal structure distortion induced by Pd-doping in FeRh alloys on the order of phase transition will be specified too.

## 5. Conclusions

The paper presents ab initio calculations and experimental studies of the correlation between the structural and magnetic properties of the Pd-doped FeRh alloys. Based on the comparative analysis of obtained results the main driving forces of the metamagnetic AFM-FM transition in the exanimated system were determined.

The calculations results revealed a tendency towards tetragonalization of the alloy crystal lattice under substitution of Rh atoms with Pd ones. The theoretical estimations of lattice parameters and nearest neighbors distance were confirmed using EXAFS analysis. In particular, an increase in the interatomic distance between the first and second nearest neighbors of palladium leads to a decrease in Fe atom magnetic moment without a noticeable change of Rh and Pd ones. This change in the spin subsystem energy origins a decrease in the energy of the phonon subsystem necessary to initiate a first-order phase transition, which, in turn, determines the AFM-FM phase transition temperature. Thus, the influence of the structural fluctuations of the magnetic subsystem was determined.

By means of electronic structure exploration it was found that the formation of the magnetic moment of the Rh/Pd is governed by the strong covalence between them and the polarized spin states of the first neighboring Fe atoms.

The impact of the $\gamma$-phase (B1 structure) presence together with its magnetic behavior on the metamagnetic phase transition, occurred in this system was comprehensively studied. In the beginning, the paramagnetic state for $\gamma$–phase was determined using two different approaches: total energy estimation and LDOS diagram constructing.

A decrease of the $\gamma$-phase volume fraction with Pd content increase was experimentally discovered. The latter is likely predetermined in $Fe_{49}Rh_{51-x}M_x$ alloys with the radius difference of the third (doping) atom in comparison with Rh atoms. This factor is considered for the first time in our paper in addition to the already mentioned influence of the quenching rate during sample preparation [40]. Additionally, the correlation between the $\gamma$-phase volume fraction and the width of the temperature hysteresis was revealed.

## CRediT authorship contribution statement

**Aleksei Komlev:** Formal analysis: Equal, Investigation: Lead, Methodology: Equal, Visualization: Lead, Writing – original draft: Lead, Validation: Equal, **Dmitriy Y. Karpenkov:** Formal analysis: Equal, Funding acquisition: Equal, Investigation: Supporting, Writing – review & editing: Lead. **Radel R. Gimaev:** Data curation: Equal, Project administration: Equal. **Alisa Chirkova:** Data curation: Equal, Formal analysis: Equal, Writing – review & editing: Supporting. **Ayaka Akiyama:** Investigation: Equal, Methodology: Equal, Visualization: Equal. **Takafumi Miyanaga:** Investigation: Equal, Visualization: Equal, Writing – review & editing: Equal, Funding acquisition: Equal. **Marcio Ferreira Hupalo:** Investigation: Equal, Writing – review & editing: Supporting. **D.J.M. Aguiar:** Investigation: Equal, Writing – review & editing: Supporting. **A.M.G. Carvalho:** Investigation: Equal, Writing – review & editing: Supporting. **María Julia Jiménez:** Funding acquisition: Equal, Software: Lead, Writing – original draft: Equal, Visualization: Equal. **Gabriela F. Cabeza:** Funding acquisition: Equal, Software: Lead, Writing – original draft: Equal, Visualization: Equal. **Vladimir I. Zverev:** Data curation: Lead, Project administration: Lead, Visualization: Equal, Writing – review & editing: Equal. **Nikolai S. Perov:** Formal analysis: Lead, Methodology: Lead, Project administration: Lead, Supervision: Lead, Writing – review & editing: Equal, Funding acquisition: Equal.

## Declaration of Competing Interest

The authors declare that they have no known competing financial interests or personal relationships which have or could be perceived to have influenced the work reported in this article.

## Acknowledgments

## Appendix A. Supporting information

Supplementary data associated with this article can be found in the online version at doi:10.1016/j.jallcom.2021.163092.

## References

[1] M. Fallot, The alloys of iron with metals of the platinum family, Ann. Phys. 10 (1938) 291–332, https://doi.org/10.1051/anphys/193811100291

[2] G. Shirane, R. Nathans, C.W. Chen, Magnetic moments and unpaired spin densities in the Fe-Rh alloys, Phys. Rev. 134 (1964) A1547–A1553, https://doi.org/10.1103/PhysRev.134.A1547

[3] J.A. Ricodeau, D. Melville, Model of the antiferromagnetic-ferromagnetic transition in FeRh alloys, J. Phys. F: Met. Phys. 2 (1972) 337–350, https://doi.org/10.1088/0305-4608/2/2/024

[4] C. Kittel, Model of exchange-inversion magnetization, Phys. Rev. 120 (1960) 335–342, https://doi.org/10.1103/PhysRev.120.335

[5] M.E. Gruner, E. Hoffmann, P. Entel, Instability of the rhodium magnetic moment as the origin of the metamagnetic phase transition in α–FeRh, Phys. Rev. B 67 (2003) 064415, https://doi.org/10.1103/PhysRevB.67.064415

[6] G. Ju, J. Hohlfeld, B. Bergman, R.J.M. van de Veerdonk, O.N. Mryasov, J.-Y. Kim, X. Wu, D. Weller, B. Koopmans, Ultrafast generation of ferromagnetic order via a laser-induced phase transformation in FeRh thin films, Phys. Rev. Lett. 93 (2004) 197403, https://doi.org/10.1103/PhysRevLett.93.197403

[7] L.M. Sandratskii, P. Mavropoulos, Magnetic excitations and femtomagnetism of FeRh: a first-principles study, Phys. Rev. B. 83 (2011) 174408, https://doi.org/10.1103/PhysRevB.83.174408

[8] H. Miyajima, S. Yuasa, Y. Otani, First-order magnetic phase transitions observed in bct FeRh-Pt, Pd Systems, Jpn. J. Appl. Phys. 32 (1993) 232, https://doi.org/10.7567/JJAPS.32S3.232

[9] G. Shirane, C.W. Chen, P.A. Flinn, R. Nathans, Hyperfine fields and magnetic moments in the Fe–Rh system, J. Appl. Phys. 34 (1963) 1044–1045, https://doi.org/10.1063/1.1729362

[10] E.F. Bertaut, A. Delapalme, F. Forrat, G. Roult, F.D. Bergevin, R. Pauthenet, Magnetic structure work at the nuclear center of grenoble, J. Appl. Phys. 33 (1962) 1123–1124, https://doi.org/10.1063/1.1728627

[11] N. Kunitomi, M. Kohgi, Y. Nakai, Diffuse scattering of neutrons in the antiferromagnetic phase of FeRh, Phys. Lett. A 37 (1971) 333–334, https://doi.org/10.1016/0375-9601(71)90695-5

[12] Cs Hargitai, On the aligned magnetic moment of the Rh atoms in the FeRh alloy, Phys. Lett. 17 (1965) 178–179, https://doi.org/10.1016/0031-9163(65)90467-1

[13] P.M. Derlet, Landau-Heisenberg Hamiltonian model for FeRh, Phys. Rev. B 85 (2012) 174431, https://doi.org/10.1103/PhysRevB.85.174431

[14] S. Polesya, S. Mankovsky, D. Ködderitzsch, J. Minár, H. Ebert, Finite-temperature magnetism of FeRh compounds, Phys. Rev. B 93 (2016) 024423, https://doi.org/10.1103/PhysRevB.93.024423

[15] A.J. Heeger, Pressure dependence of the FeRh first-order phase transition, J. Appl. Phys. 41 (1970) 4751–4752, https://doi.org/10.1063/1.1658533

[16] L.I. Vinokurova, A.V. Vlasov, M. Pardavi-Horváth, Pressure effects on magnetic phase transitions in FeRh and FeRhIr alloys, Phys. Status Solidi B 78 (1976) 353–357.

[17] R.C. Wayne, Pressure dependence of the magnetic transitions in Fe-Rh alloys, Phys. Rev. 170 (1968) 523–527, https://doi.org/10.1103/PhysRev.170.523

[18] K. Kamenev, Z. Arnold, J. Kamarád, N.V. Baranov, Pressure induced antiferromagnetism in (Fe1−xNix)49Rh51 alloys, J. Alloy. Compd. 252 (1997) 1–5, https://doi.org/10.1016/S0925-8388(96)02710-7

[19] J.S. Kouvel, Unusual nature of the abrupt magnetic transition in FeRh and its pseudobinary variants, J. Appl. Phys. 37 (1966) 1257–1258, https://doi.org/10.1063/1.1708424

[20] P.H.L. Walter, Exchange inversion in ternary modifications of iron rhodium, J. Appl. Phys. 35 (1964) 938–939, https://doi.org/10.1063/1.1713547

[21] S. Yuasa, H. Miyajima, Y. Otani, Magneto-volume and tetragonal elongation effects on magnetic phase transitions of body-centered tetragonal FeRh1-xPtx, J. Phys. Soc. Jpn. 63 (1994) 3129–3144, https://doi.org/10.1143/JPSJ.63.3129

[22] S. Yuasa, H. Miyajima, Y. Otani, K. Tsuji, Y. Katayama, K. Kusumi, H. Yokoyama, K. Yaoita, O. Shimomura, First-order magnetic phase transition in bcc FeRh–Ir alloy under high pressures up to 6.2 GPa, J. Phys. Soc. Jpn. 63 (1994) 855–858, https://doi.org/10.1143/JPSJ.63.855

[23] N.V. Baranov, E.A. Barabanova, Electrical resistivity and magnetic phase transitions in modified FeRh compounds, J. Alloy. Compd. 219 (1995) 139–148, https://doi.org/10.1016/0925-8388(94)01375-6

[24] M.R. Ibarra, P.A. Algarabel, C. Marquina, Y. Otani, S. Yuasa, H. Miyajima, Giant room temperature volume magnetostriction in an Fe·Rh·Pd alloy, J. Magn. Magn. Mater. 140–144 (1995) 231–232, https://doi.org/10.1016/0304-8853(94)01442-6

[25] P. Kushwaha, A. Lakhani, R. Rawat, P. Chaddah, Low-temperature study of field-induced antiferromagnetic-ferromagnetic transition in Pd-doped Fe-Rh, Phys. Rev. B 80 (2009) 174413, https://doi.org/10.1103/PhysRevB.80.174413

[26] P. Kushwaha, A. Lakhani, R. Rawat, P. Chaddah, Influence of thermal annealing and magnetic field on first order magnetic transition in Pd substituted FeRh, J. Phys.: Conf. Ser. 200 (2010) 032038, https://doi.org/10.1088/1742-6596/200/3/032038

[27] V.I. Zverev, R.R. Gimaev, T. Miyanaga, A.A. Vaulin, A.F. Gubkin, B.B. Kovalev, A.M. dos Santos, E. Lovell, L.F. Cohen, N.A. Zarkevich, Peculiarities of the phase transformation dynamics in bulk FeRh based alloys from magnetic and structural measurements, J. Magn. Magn. Mater. (2020) 167560, https://doi.org/10.1016/j.jmmm.2020.167560

[28] S. Yuasa, H. Miyajima, Y. Otani, G. Masada, N. Wakabayashi, K. Tajima, X-ray diffraction studies of FeRh0.38Pd0.62 alloy with orthorhombic structure, J. Phys. Soc. Jpn. 64 (1995) 3153–3156, https://doi.org/10.1143/JPSJ.64.3153

[29] S. Yuasa, Y. Otani, H. Miyajima, A. Sakuma, Magnetic properties of bcc FeRh1-xMx systems, IEEE Transl. J. Magn. Jpn. 9 (1994) 202–209, https://doi.org/10.1109/TJMJ.1994.4565981

[30] T. Fukuda, T. Kakeshita, Martensitic transformation in Pd doped FeRh exhibiting a metamagnetic transition, J. Alloy. Compd. 563 (2013) 192–196, https://doi.org/10.1016/j.jallcom.2013.02.029

[31] Y. Yokoyama, M. Usukura, S. Yuasa, Y. Suzuki, H. Miyajima, T. Katayama, MFM observation of magnetic phase transitions in ordered FeRh systems, J. Magn. Magn. Mater. 177–181 (1998) 181–182, https://doi.org/10.1016/S0304-8853(97)00953-0

[32] C.J. Kinane, M. Loving, M.A. de Vries, R. Fan, T.R. Charlton, J.S. Claydon, D.A. Arena, F. Maccherozzi, S.S. Dhesi, D. Heiman, C.H. Marrows, L.H. Lewis, S. Langridge, Observation of a temperature dependent asymmetry in the domain structure of a Pd-doped FeRh epilayer, New J. Phys. 16 (2014) 113073, https://doi.org/10.1088/1367-2630/16/11/113073

[33] T. Miyanaga, T. Itoga, T. Okazaki, K. Nitta, Local structural change under antiferro- and ferromagnetic transition in FeRh alloy, J. Phys.: Conf. Ser. 190 (2009) 012097, https://doi.org/10.1088/1742-6596/190/1/012097

[34] Y. Wakisaka, Y. Uemura, T. Yokoyama, H. Asakura, H. Morimoto, M. Tabuchi, D. Ohshima, T. Kato, S. Iwata, Anomalous structural behavior in the metamagnetic transition of FeRh thin films from a local viewpoint, Phys. Rev. B. 92 (2015) 184408, https://doi.org/10.1103/PhysRevB.92.184408

[35] L.H. Lewis, C.H. Marrows, S. Langridge, Coupled magnetic, structural, and electronic phase transitions in FeRh, J. Phys. D: Appl. Phys. 49 (2016) 323002, https://doi.org/10.1088/0022-3727/49/32/323002

[36] R.R. Gimaev, A.A. Vaulin, A.F. Gubkin, V.I. Zverev, Peculiarities of magnetic and magnetocaloric properties of Fe–Rh alloys in the range of antiferromagnet–ferromagnet transition, Phys. Met. Metallogr. 121 (2020) 823–850, https://doi.org/10.1134/S0031918×20090045

[37] A. Chirkova, F. Bittner, K. Nenkov, N.V. Baranov, L. Schultz, K. Nielsch, T.G. Woodcock, The effect of the microstructure on the antiferromagnetic to ferromagnetic transition in FeRh alloys, Acta Mater. 131 (2017) 31–38, https://doi.org/10.1016/j.actamat.2017.04.005

[38] L.J. Swartzendruber, The Fe−Rh (Iron-Rhodium) system, Bull. Alloy Phase Diagr. 5 (1984) 456–462, https://doi.org/10.1007/BF02872896

[39] I. Ohnuma, T. Gendo, R. Kainuma, G. Inden, K. Ishida, Phase equilibria and thermodynamic evaluation approximating short-range ordering energy in the Fe–Rh binary system, ISIJ Int. 49 (2009) 1212–1219, https://doi.org/10.2355/isijinternational.49.1212

[40] M. Takahashi, R. Oshima, Annealing effect on phase transition of equiatomic FeRh alloy, Mater. Trans. JIM 36 (1995) 735–742, https://doi.org/10.2320/matertrans1989.36.735

[41] O. Pavlukhina, V. Sokolovskiy, V. Buchelnikov, M. Zagrebin, Structural, magnetic and electronic properties of FeRhxPd1-x compounds: Ab initio study, Phys. B: Condens. Matter 578 (2020) 411882, https://doi.org/10.1016/j.physb.2019.411882

[42] M.J. Jiménez, A.S. Komlev, R.R. Gimaev, V.I. Zverev, G.F. Cabeza, Electronic and thermoelectric properties of FeRh Pd-doped alloys: Ab initio study, J. Magn. Magn. Mater. 538 (2021) 168258, https://doi.org/10.1016/j.jmmm.2021.168258

[43] A. Hernando, E. Navarro, A.R. Yavari, D. Fiorani, M. Rosenberg, Magnetic properties of disordered grain boundaries in nanocrystalline FeRh alloys, J. Magn. Magn. Mater. 203 (1999) 223–225, https://doi.org/10.1016/S0304-8853(99)00247-4

[44] M.L. Arreguín-Hernández, C.F. Sánchez-Valdés, J.L.S. Llamazares, D. Ríos-Jara, V.K. Pecharsky, M.I. Blinov, V.N. Prudnikov, B.B. Kovalev, V.I. Zverev, A.M. Tishin, Magnetoelastic transition and magnetocaloric effect in induction melted Fe100−xRhx bulk alloys with x = 50, 51, J. Alloy. Compd. 871 (2021) 159586, https://doi.org/10.1016/j.jallcom.2021.159586

[45] V. Rodionov, A. Amirov, M. Annaorazov, E. Lähderanta, A. Granovsky, A. Aliev, V. Rodionova, Thermal hysteresis control in Fe49Rh51 alloy through annealing process, Processes 9 (2021) 772, https://doi.org/10.3390/pr9050772

[46] V.I. Zverev, A.M. Saletsky, R.R. Gimaev, A.M. Tishin, T. Miyanaga, J.B. Staunton, Influence of structural defects on the magnetocaloric effect in the vicinity of the first order magnetic transition in Fe50.4Rh49.6, Appl. Phys. Lett. 108 (2016) 192405, https://doi.org/10.1063/1.4949355

[47] B. Ravel, M. Newville, ATHENA, ARTEMIS, HEPHAESTUS: data analysis for X-ray absorption spectroscopy using IFEFFIT, J. Synchrotron Radiat. 12 (2005) 537–541, https://doi.org/10.1107/S0909049505012719

[48] G. Kresse, J. Hafner, Ab initio molecular dynamcis for liquid metals, Phys. Rev. B 47 (1993) 558–561.

[49] G. Kresse, J. Hafner, Ab initio molecular dynamics for open-shell transition metals, Phys. Rev. B 48 (1993) 13115–13118, https://doi.org/10.1103/PhysRevB.48.13115

[50] G. Kresse, J. Furthmüller, J. Hafner, Ab initio molecular-dynamics simulation of the liquid-metal–amorphous-semiconductor transition in germanium, Phys. Rev. B 49 (1994) 14251–14269, https://doi.org/10.1016/0927-0256(96)00008-0

[51] J. Hafner, Ab-initio simulations of materials using VASP: density-functional theory and beyond, J. Comput. Chem. 29 (2008) 2044–2078, https://doi.org/10.1002/jcc.21057

[52] P.E. Blöchl, Projector augmented-wave method, Phys. Rev. B 50 (1994) 17953–17979, https://doi.org/10.1103/PhysRevB.50.17953

[53] J.P. Perdew, K. Burke, M. Ernzerhof, Generalized gradient approximation made simple, Phys. Rev. Lett. 77 (1996) 3865–3868, https://doi.org/10.1103/PhysRevLett.77.3865

[54] M. Methfessel, A.T. Paxton, High-precision sampling for Brillouin-zone integration in metals, Phys. Rev. B 40 (1989) 3616–3621, https://doi.org/10.1103/PhysRevB.40.3616

[55] V. Wang, N. Xu, J.C. Liu, G. Tang, W.-T. Geng, VASPKIT: A User-friendly Interface Facilitating High-throughput Computing and Analysis Using VASP Code, ArXiv:1908.08269 [Cond-Mat]. (2020). ⟨http://arxiv.org/abs/1908.08269⟩ (Accessed 20 April 2021).

[56] M.J. Jiménez, A.B. Schvval, G.F. Cabeza, Ab initio study of FeRh alloy properties, Comput. Mater. Sci. 172 (2020) 109385, https://doi.org/10.1016/j.commatsci.2019.109385

[57] C.F. Sánchez-Valdés, R.R. Gimaev, M. López-Cruz, J.L. Sánchez Llamazares, V.I. Zverev, A.M. Tishin, A.M.G. Carvalho, D.J.M. Aguiar, Y. Mudryk, V.K. Pecharsky, The effect of cooling rate on magnetothermal properties of Fe49Rh51, J. Magn. Magn. Mater. 498 (2020) 166130, https://doi.org/10.1016/j.jmmm.2019.166130

[58] F. Scheibel, T. Gottschall, A. Taubel, M. Fries, K.P. Skokov, A. Terwey, W. Keune, K. Ollefs, H. Wende, M. Farle, M. Acet, O. Gutfleisch, M.E. Gruner, Hysteresis design of magnetocaloric materials—from basic mechanisms to applications, Energy Technol. 6 (2018) 1397–1428, https://doi.org/10.1002/ente.201800264